

<https://doi.org/10.1038/s44384-025-00033-6>

Broadband enhancement and suppression of backscattering from objects in shallow-sea waveguides through the prescription of incident wavefronts

Tengjiao He^{1,2,4}✉ & Wei Guo^{3,4}✉

This paper presents a methodology for enhancing and suppressing backscattering from submerged objects in shallow-water waveguides. A hybrid numerical model is developed that integrates a two-step finite element method (FEM) and a normal mode (NM) algorithm. The FEM scheme computes the near-field scattered field generated by an elastic structure under non-plane-wave incident conditions in a shallow-water environment. A modal filter technique is then applied to construct the modal-domain reflection and transmission matrices of the scattering region using the near-field data derived from the FEM. Scattering enhancement and suppression are achieved by maximizing the Rayleigh quotient of these matrices, with the prescribed incident wavefront determined via singular-value decomposition. The scattered field is subsequently reconstructed using the prescribed wavefront and the NM algorithm. Validation of the hybrid model is performed through comparison with a direct FEM simulation for an elastic spherical shell. Further simulations are conducted for realistic scenarios involving multiple spherical scatterers and a benchmark submarine model. The results demonstrate that the proposed method enables broadband control of backscattering in shallow-water waveguides.

Active sonar systems are widely employed in underwater acoustic imaging, localization, and detection. They rely on the analysis of a target's scattered field to infer its geometric and material properties¹. The performance of these systems is critically dependent on the scattering strength, and this fact has driven significant research interest in scattering control methodologies^{2–5}. Conventionally, the scattering strength can be amplified by prescribing a directional beam and optimizing the incident wave's direction. However, in shallow-water environments, typical operational domains for active sonar, the incident field deviates from plane-wave behavior due to boundary interactions and sound speed inhomogeneities⁶, which complicate scattered field control. A critical research challenge involves controlling backscatter in such environments to optimize active sonar performance.

Directional beams facilitate the precise control of scattered fields by prescribing the incident wavefronts⁷. When a directional beam is introduced

into a shallow-water waveguide, the sound propagation exhibits distinct beam patterns over short ranges and modal interference over longer ranges^{8,9}. Consequently, manipulating the incident wavefronts within a waveguide is a significant challenge, particularly when attempting to enhance either backward or forward scattering from objects within the waveguide. Nevertheless, maximal flux transmission in inhomogeneous acoustic waveguides can be achieved through singular value decomposition (SVD) of the transmission matrix^{10,11}. By applying SVD to the transmission matrix, the right singular vector associated with the maximum singular value, corresponding to the peak energy transmission ratio^{12,13}, can be identified as the optimal incident wavefront to achieve unity flux transmittance through the waveguide. This phenomenon was first observed in mesoscopic electron transport studies¹⁴ and was later investigated for enhancing optic transmission^{15–17}, where open channels (characterized by complete transmission) and closed channels (exhibiting total reflection)

¹Key Laboratory of Marine Intelligent Equipment and System, Ministry of Education, Shanghai Jiao Tong University, Shanghai, PR China. ²School of Ocean and Civil Engineering, Shanghai Jiao Tong University, Shanghai, PR China. ³College of Meteorology and Oceanography, National University of Defense Technology, Changsha, PR China. ⁴These authors contributed equally: Tengjiao He, Wei Guo. ✉e-mail: hetengjiao@sjtu.edu.cn; guowei23@nudt.edu.cn

form the fundamental basis for field solutions within lossless scattering media¹⁸.

The objectives of this study are twofold. First, we introduce the concept of backscattering manipulation in inhomogeneous waveguides to the field of underwater acoustics. By identifying the incident wavefront through SVD of the reflection and transmission matrices associated with the scattering region where a target is positioned, the scattered field can be systematically manipulated. Second, we develop a hybrid numerical model that integrates a two-step finite element method (FEM) to compute the near-field distribution within the scattering region and a normal mode (NM) algorithm⁸ to predict far-field scattering patterns using the near-field data. Our hybrid model addresses a gap in existing research, as no prior numerical model has been reported for constructing reflection and transmission matrices in shallow-water waveguides containing arbitrary scatterers, to the best of the authors' knowledge. Furthermore, the proposed model enables the analysis of scattering problems involving non-plane-wave incident fields, a critical feature for shallow-water applications where incident wavefronts exhibit significant interference effects⁶.

Our hybrid model allows for the manipulation of backward scattering from objects in shallow-water waveguides. As shown in Fig. 1, our custom two-step FEM scheme computes scattered fields for arbitrary scatterers in shallow-water environments with non-plane-wave excitations. Specifically, the extraction of near-field data from the finite element (FE) model allows the formulation of reflection and transmission matrices in the modal domain (**R** and **T**). These matrices are analyzed via SVD to identify the incident wavefront resulting in maximal reflection or transmission in the waveguide. The prescribed wavefront corresponds to the right singular vector associated with the largest singular value and is applied to predict far-field scattering using a NM algorithm. Unlike existing studies on Fano scattering in inhomogeneous waveguides^{19–21}, which rely on resonance between the incident wavefront and the local structure²², our method offers the advantage of prescribing wavefronts at arbitrary frequencies. In contrast, Fano scattering achieves maximal reflection or transmission only at resonance frequencies, limiting its practicality for active sonar performance enhancement.

This paper is organised as follows: we provide *in silico* proof-of-principle, exploration of the proposed method for manipulating backscattering from objects in shallow-sea waveguides through the prescription of incident wavefronts. We start with a numerical validation of the proposed two-step FEM through the analysis of spherical scatterers in a Pekeris waveguide. Next the backscattering manipulation of a single spherical shell is demonstrated, after which the scenario of double spherical shells and a more complex but practical case involving a benchmark submarine model are presented. We then discuss the underlying mechanism of incident wavefront prescription. A comprehensive parametric study is also performed to investigate the influences of the scale and the material of the scatterer and the influence of the environment on the scattering manipulation. Finally, we provide practical guidelines for implementing the proposed method and conclude by outlining the theoretical framework and algorithms. These methodologies include the principles of reflection and transmission optimization in inhomogeneous waveguides, the development of a two-step FEM formulation, the construction of reflection/transmission matrices, and the implementation of a NM algorithm for scattered-field computation.

Results

Model validation

In this study, a hybrid numerical model, illustrated in Fig 1a, is employed to construct **R** and **T** by means of modal filtering (see Methods). The near-field region is modeled using a two-step FEM, where the incident field distribution is obtained using a NM algorithm⁸. As shown in Fig 1b, the FE model consists of two steps (see Methods). First, the NM algorithm is used to compute the incident field distribution, specifically, v_{inc} (normal velocity) and p_{inc} (pressure), on the object's surface Γ_{s-a} . By prescribing $-v_{inc}$ on Γ_{s-a} , the geometric scattering from the object can be predicted, yielding the surface pressure load distribution p_g . In the second step, p_g and p_{inc} are

jointly applied as surface pressure loads on Γ_{s-a} , exciting the elastic object to vibrate and radiate acoustic waves into the surrounding fluid. Accordingly, only the pressure acoustics module is used in the first step, while the second step requires a coupled acoustic-solid interaction module. The FEM solver produces the near-field scattering from the object, which is then integrated with the NM algorithm to predict far-field scattering. As illustrated in Fig 1a, a slice parallel to the incident wavefront is first identified. The scattered field is then extracted along a vertical line extending from the sea surface to the truncation depth defined by the perfectly matched layer (PML), in both the backscattered and forward-scattered directions. This field is subsequently used to construct **R** and **T** and to compute the far-field scattering using the NM algorithm (see Methods).

Before performing the backscattering manipulation using the proposed model, we validate it through comparison with a benchmark solution. This validation study serves two primary objectives. First, we establish a coupled acoustic-structural FE model to verify the accuracy of the proposed FEM framework for predicting elastic scattered fields under arbitrary waveguide excitations. This benchmark employs identical geometric and material parameters as the proposed two-step FEM scheme, and a single mode excitation is prescribed for both cases as the incident field. In the benchmark solution, cylindrical wave radiation boundary conditions with depth-dependent amplitudes determined by the NM shape functions $\phi_n(z)$ are implemented at the outer boundary. Such an incident field is formed using an equivalent sound speed of $\omega/k_{r,n}$ (where ω represents the angular frequency, and $k_{r,n}$ denote the eigenvalue), with a virtual source position r_s chosen to ensure alignment between modal excitation and the scatterer's horizontal position. The incident waves come from the $-y$ direction along the y -axis. The scatterer is placed at (0 m, 1000 m, 35 m), giving $r_s = 1000$ m. The benchmark and proposed model radii are set to 100 m and 50 m, respectively. The shallow-water waveguide parameters are provided in Table 1. Figure 2a, b illustrate the FE model and the associated meshing scheme for a spherical scatterer. Further detail about the FEM implementations can be found in Methods.

First, the effectiveness of the proposed model in computing the near-field scattering is validated. Figure 2d compares results at 100 Hz for Mode 1 excitation. Analysis of the $x=0$ plane reveals strong near-field agreement ($|y| < 50$ m), which is further supported by the normalized pressure extracted on a 30 m-radius circle surrounding the scatterer [Fig. 2c].

Second, the validation study demonstrates the efficacy of the far-field scattering prediction. Far-field predictions between 50 m and 100 m are computed using the modal filtering based on near-field data derived from the two-step FEM. As shown in Fig 2d, consistent far-field agreement ($|y| > 50$ m) confirms the prediction accuracy. Minor discrepancies below the water-seabed interfaces ($y = \pm 50$ m) likely arise from truncated leaky wave components in modal representations, though the water-column results remain unaffected by these evanescent modes. This divergence does not impact the validity of the model for underwater applications.

Manipulation of backward scattering from a steel spherical shell

The enhancement and suppression of backscattering from elastic objects in shallow water starts with optimizing the Rayleigh quotient of **R** and **T** (see Methods). We construct **R** and **T** using the modal filter technique based on the data extracted from the proposed two-step FEM (see Methods). Using this method, we investigate the enhancement and suppression of backscattering from the steel spherical shell in shallow-water environments (see FEM implementation in Methods for the detailed parameters of the scatterer). The shell is located at coordinates (0 m, 500 m, 35 m), where $y = 0$ m corresponds to the horizontal position of the source. Simulations are conducted at 215 Hz, incorporating 32 modes in the computation (including 16 propagating and 16 leaky modes).

To evaluate the effectiveness of the proposed method for backscattering control, we begin by analyzing backscatter enhancement from the shell in the Pekeris waveguide. To elucidate how backscatter enhancement arises, we first explain the minimal diffraction by comparing both the

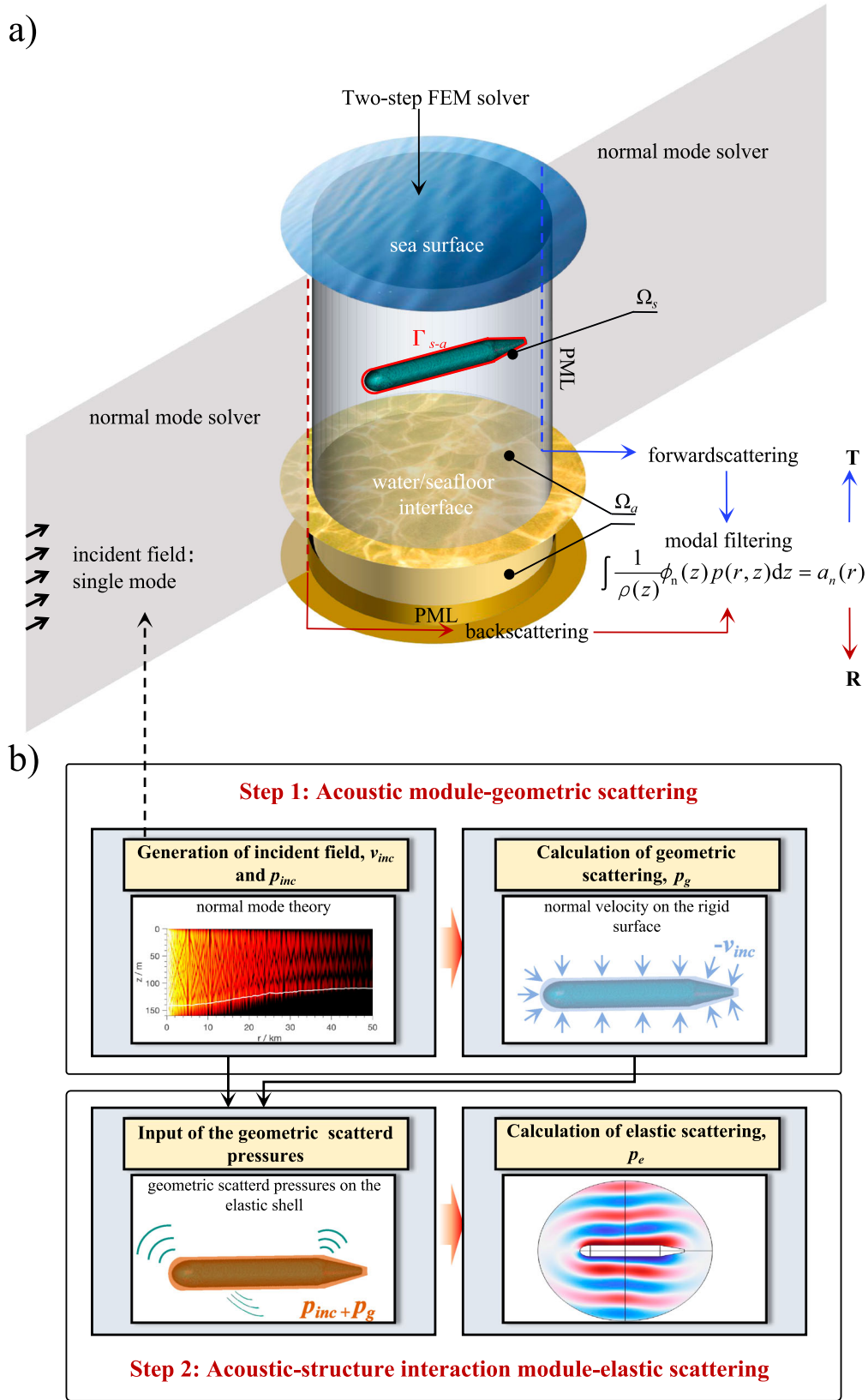


Fig. 1 | Theoretical model that integrates a two-step FEM and a NM algorithm. **a** A schematic of the FE model implemented in the proposed two-step FEM scheme for solving the scattering from an arbitrary elastic structure in a two-layered, fluid waveguide. Also shown is the process of computing the scattered field using the

coupled FEM/NM method, where the near-field pressures distributed over a vertical line, generated by the two-step FEM solver, are extracted to construct \mathbf{R} and \mathbf{T} . **b** A flow chart for the proposed two-step FEM scheme.

incident and scattered field pressures. Next, the total field exhibiting the enhanced backscattering from the shell can be obtained by superposing the incident and scattered fields. Figure 3a illustrates the prescribed incident field (the real part of the pressure) for backscattering enhancement, showing

Table 1 | Parameters of the Pekeris waveguide used in the simulations in Figs. 3–9

Parameter	Values
Water depth	70 m
Water sound speed	1500 m/s
Water density	1000 kg/m ³
Sediment thickness	30 m
Seabed sound speed	2200 m/s
Seabed sound attenuation	0.2 dB/λ
Seabed density	2000 kg/m ³

a pronounced focal region directly ahead of the shell. Notably, forward scattering from the shell cancels out the incident field at ranges beyond 500 m, where the scattered and incident fields are 180° out of phase. This phenomenon is demonstrated in the magnified plots of Fig. 3a, which display local pressure variations within the 950–1000 m range. The results confirm significant backscattering enhancement, as observed in the third row of Fig. 3a, where the forward field exhibits negligible diffraction.

In practical scenarios, scatterers are randomly positioned at varying horizontal distances. To evaluate the robustness of backscattering control, the shell is relocated to 100 m (short range) and 1000 m (long range) from the source. The sound pressure level contours shown in Fig. 3b demonstrate that the prescribed wavefronts consistently converge near the scatterer, forming a focal spot on the shell. The results for varying scatterer positions confirms the method's efficacy in backscattering control for any scatterer position.

To further demonstrate that the prescribed wavefronts serve as the optimal incident field for maximizing reflection within the waveguide, Fig. 3c compares the total fields generated by mode 1 excitation and a point

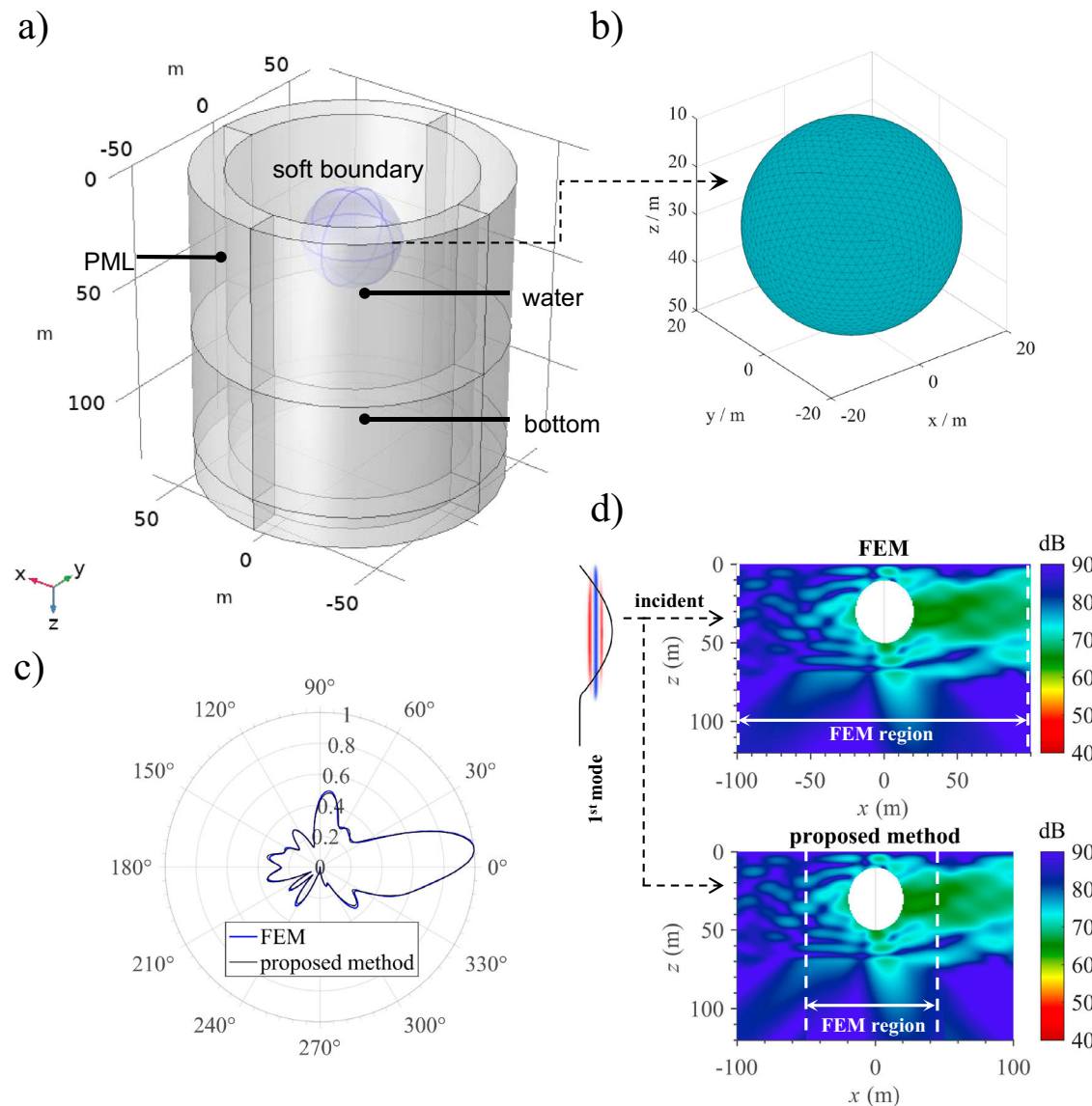


Fig. 2 | Validation of the proposed two-step FEM scheme. **a** A schematic of the FE model implemented in the proposed two-step FEM scheme, and **(b)** the detailed meshing scheme for the spherical shell considered in the simulation. **c** The normalized scattered pressures solved using the proposed model and a coupled acoustic-structural FEM model compared along the circle around the elastic spherical shell with

a radius of 30 m at 100 Hz. **d** A scattered field comparison between the two models in the $x = 0$ m plane at 100 Hz. The scattered field is excited by an individual mode (Mode 1). In the proposed model, the field within $y = \pm 50$ m is computed by the proposed two-step FEM scheme, and the field outside this region is solely solved by normal modes (NMs).

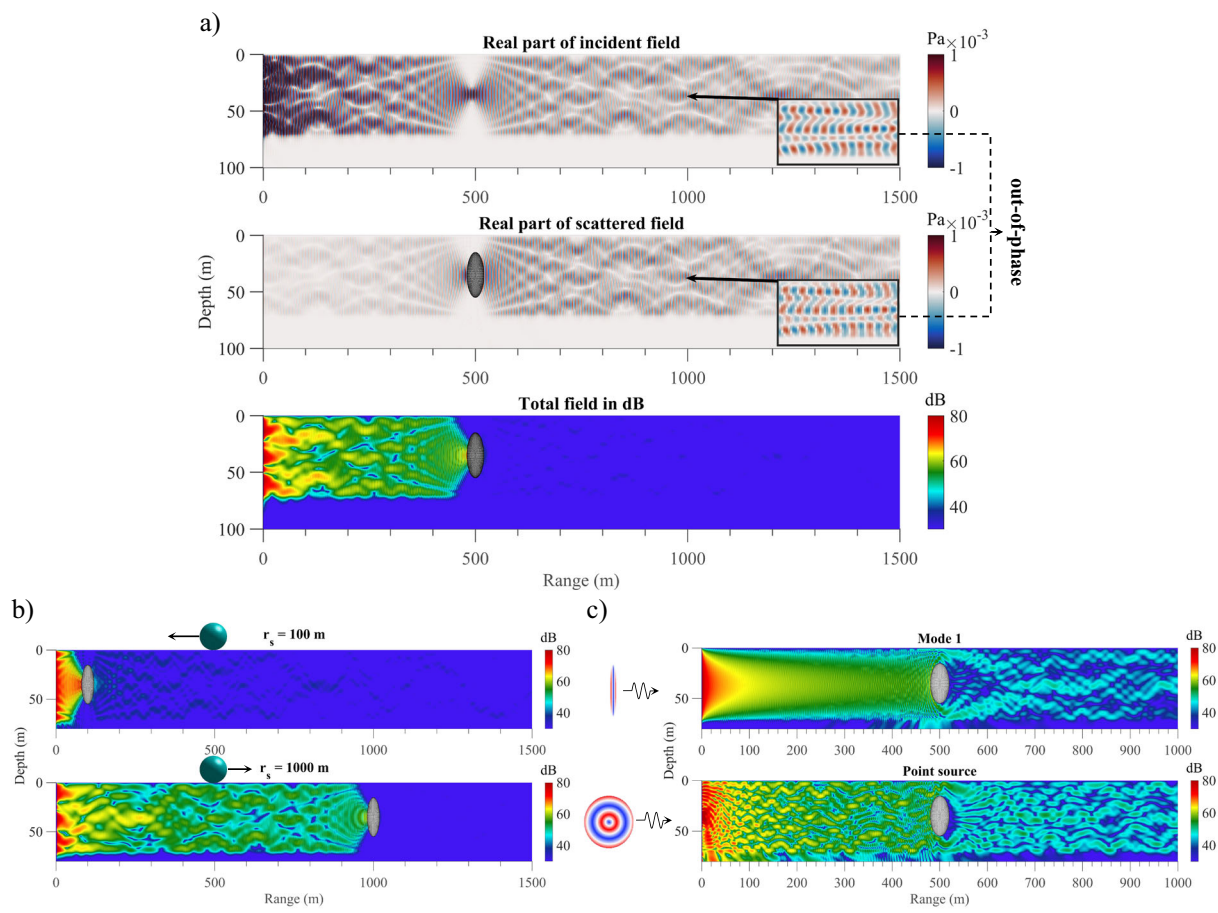


Fig. 3 | The enhancement of backscattering from a steel spherical shell in the Pekeris waveguide. a The prescribed incident field for enhancing backscattering from the steel spherical shell in the waveguide (the real part of the pressure), the scattered field due to the prescribed incident field (the real part of the pressure), and the total field when the scatterer is placed at a distance of 500 m (sound pressure

level). The magnified plots in (a) display the local region from $r = 950$ m to $r = 1000$ m, and the results are given at 215 Hz. **b** The corresponding total fields when the scatterer is placed at distances of 100 m and 1000 m, respectively. **c** The total fields resulting from the excitation of Mode 1 and a point source at 215 Hz.

source. Neither excitation achieves maximal reflection, as evidenced by significant diffraction behind the shell and the formation of a shadow zone when the prescribed wavefront is applied. For quantitative analysis, the reflection-to-incidence ratio G_r (defined in Eq. (14) in Methods) is utilized. In this study, G_r is evaluated across the FEM/NM coupling interface in the backscattering direction. The G_r values for the mode 1 and point source excitations are 36.3% and 21.8%, respectively. In contrast, G_r rises to 48.2% under prescribed wavefront excitation, demonstrating that the proposed method effectively enhances the reflected energy.

Next, we assess the effectiveness of our proposed method in backscattering control by demonstrating suppression of the backscattered field. Figure 4a depicts the prescribed incident fields for backscattering suppression when the shell is placed at three different distances (100 m, 500 m, and 1000 m). Unlike the backscattering enhancement configuration, a distinct shadow zone forms precisely at the scatterer location, characterized by minimal interaction between the incident waves and the shell. This shadow zone is formed by a quasi-Gaussian beam upon transmission past the shell. Analysis of the scattered field in this figure reveals that the peak energy density of this beam, observed at its narrowest cross-section, primarily interacts with the sea surface horizontally while making minimal contact with the shell. This interaction results in markedly weaker scattering compared to the case of backscattering enhancement, enabling maximal sound transmission through the waveguide. Again, the method's efficacy in backscattering control is confirmed

by various scatterer positions, indicating its potential in solving practical engineering problems.

The scenario of multiple scatterers

In realistic settings, the medium often contains multiple scatterers, which complicates the prescription of incident wavefronts for backscattering control. To demonstrate the effectiveness of our method for multiple scatterers, we extend the simulations to realistic scenarios involving dual spherical shells. An incident frequency of 215 Hz is applied.

Dual steel spherical shells are simulated under geometric, material and environmental parameters identical to those in the single-sphere case. The larger shell (radius 15 m) is positioned at coordinates (0 m, 490 m, 20 m), while the smaller shell (radius 10 m) is placed at (0 m, 515 m, 55 m). The two-step FEM scheme is applied within the computational domain with a radius of 30 m.

We evaluate our method's performance for backscattering control in multi-scatterer configurations by demonstrating both enhancement and suppression of the backscattered field from dual spherical shells. Figure 5 presents the corresponding results for the two-shell configuration. Under enhancement conditions, the prescribed wavefront focuses energy onto the larger shell while avoiding the smaller one. The focusing behavior results in minimal sound transmission through the waveguide and a pronounced shadow zone beyond 600 m. Conversely, the prescribed wavefronts for suppressing backscattering propagate through the path between the

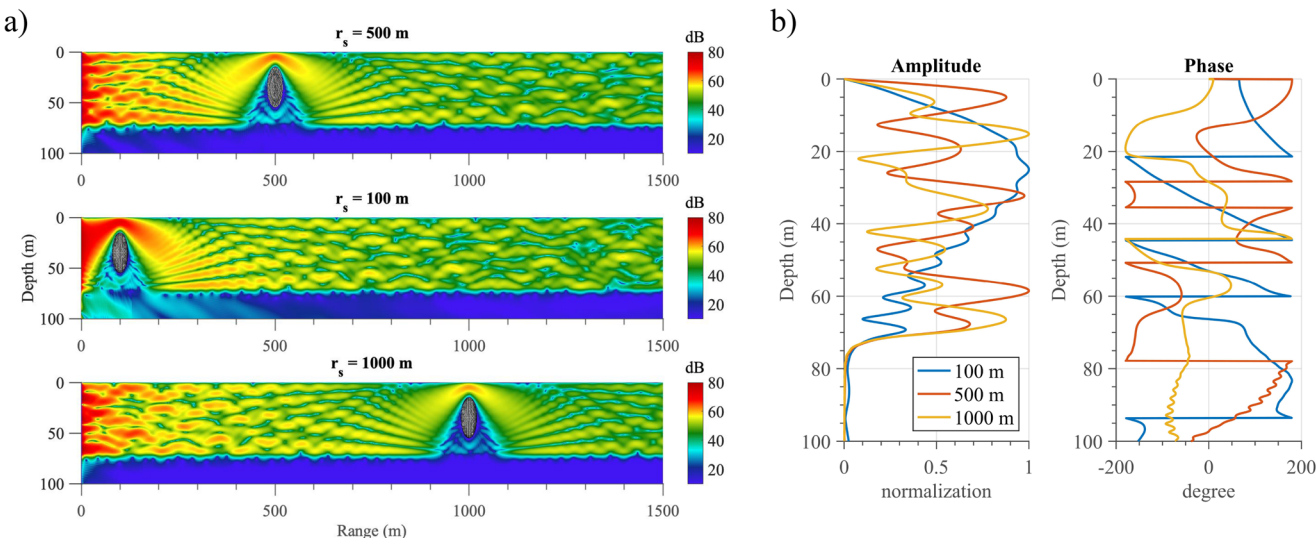


Fig. 4 | The suppression of backscattering from a steel spherical shell in the Pekeris waveguide. **a** The total fields induced by the prescribed incident fields for suppressing backscattering from the steel spherical shell at 215 Hz, with the scatterer

placed at a horizontal distance of 500 m, 100 m, and 1000 m, respectively. **b** The prescribed incident wavefronts are a function of depth for the three scatterer positions. The left and right panels show the amplitude and phase, respectively.

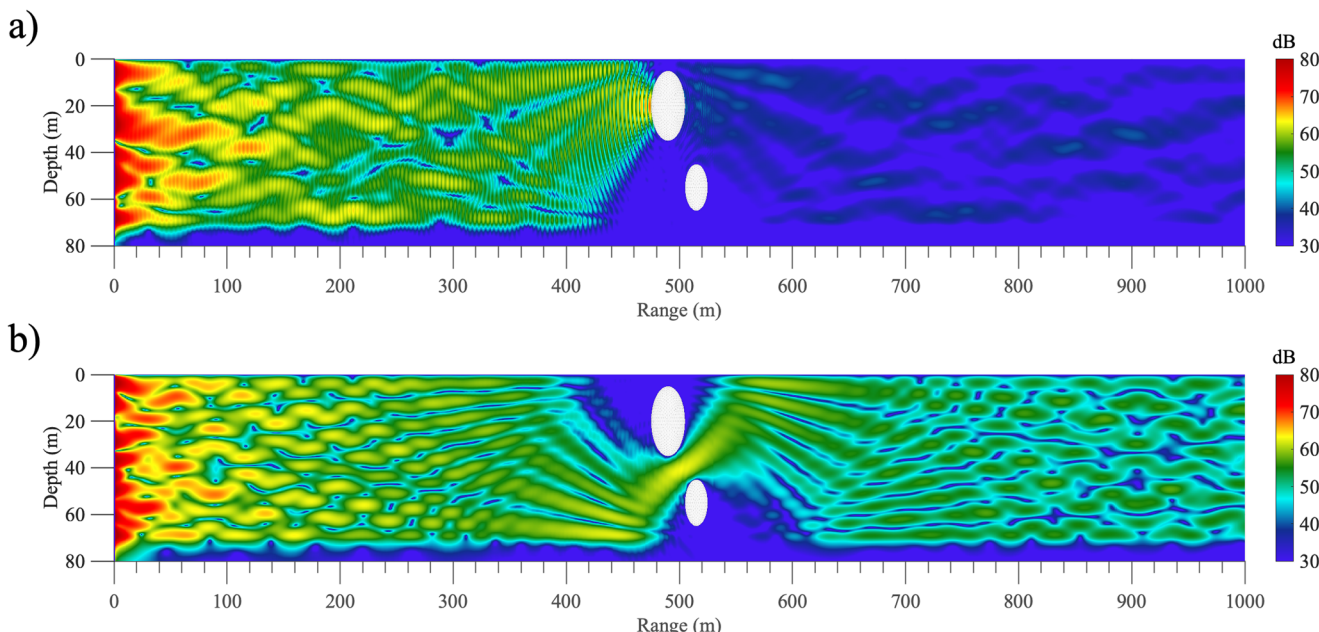


Fig. 5 | The backscattering manipulation of double spherical shells in the Pekeris waveguide. Enhancement (a) and suppression (b) of the backscattering from two steel spherical shells at 215 Hz.

scatterers, forming a converging Gaussian-like beam. This incident field minimizes interaction with the shells, enabling near-total transmission through the waveguide. These results validate the method's adaptability to complex scenarios involving multiple scatterers.

The scenario of a geometrically complex scatterer

We then analyze a geometrically complex scatterer: a Benchmark-I submarine model (length: 60 m) with the meshing scheme shown in Fig. 6a. A rigid boundary condition is applied to the submarine surface, and the environmental parameters match those in the single-sphere case. The submarine is positioned at coordinates (0 m, 500 m, 35 m). An incident frequency of 215 Hz is applied. The radius of the computational domain for the two-step FEM is 50 m.

Again, we demonstrate both enhancement and suppression of the backscattered field from the submarine model to highlight the versatility of our method for more complex scatterers. Figure 6b shows the backscattering enhancement and suppression for an incident wavefront aligned parallel to the submarine's bow. Despite the subwavelength scattering cross-section, a discernible focusing pattern forms at the bow under enhancement conditions. Conversely, suppression-directed wavefronts achieve near-total transmission through the waveguide by minimizing interaction with the scatterer. Figure 6c presents analogous results for a wavefront aligned perpendicular to the submarine's bow. In this case, the enlarged scattering cross-section intensifies the backscattering enhancement compared to Fig. 6b. These findings demonstrate the method's adaptability to realistic scenarios involving geometrically complex scatterers.

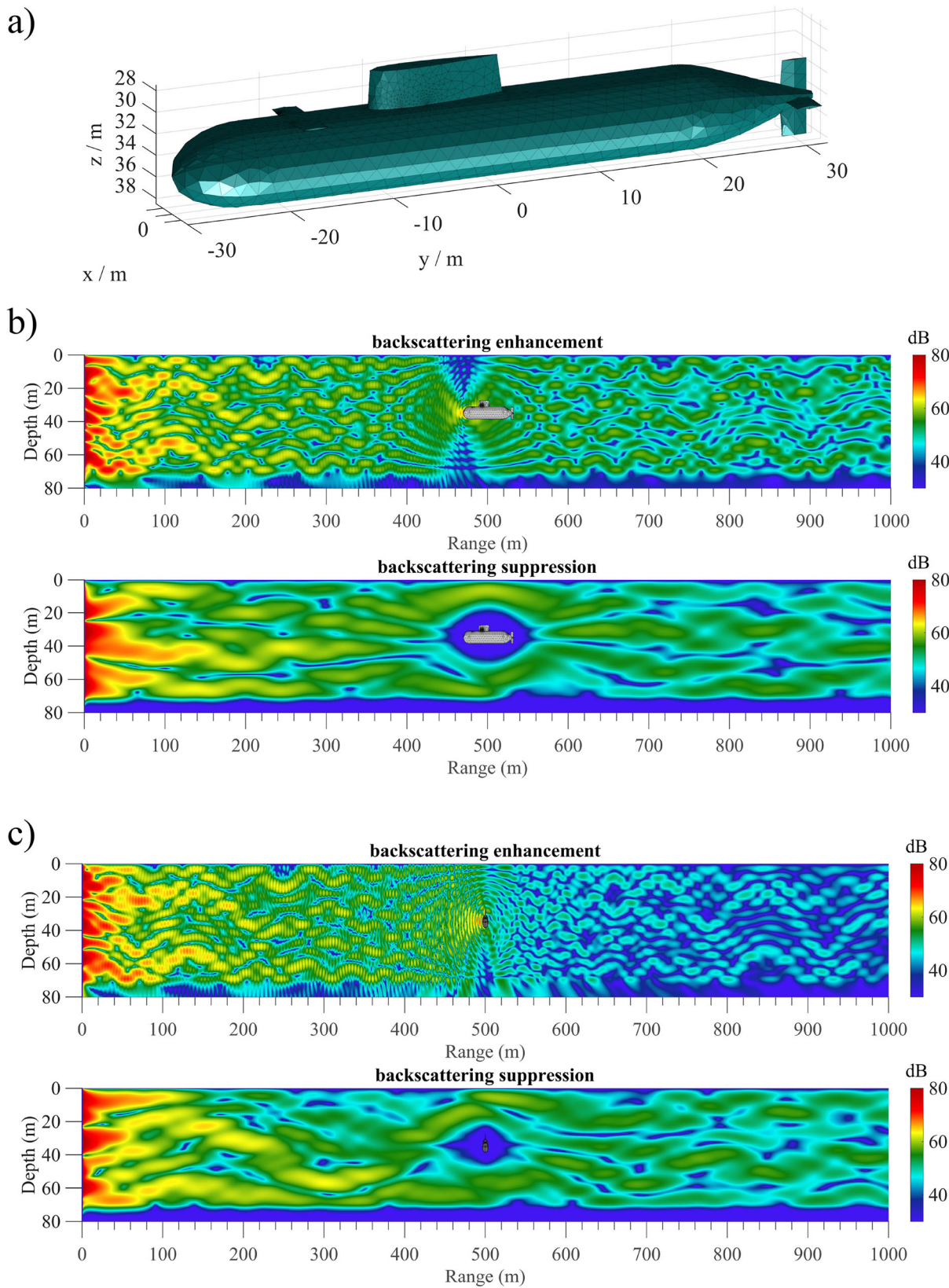


Fig. 6 | The backscattering manipulation of a submarine model in the Pekeris waveguide. **a** A schematic of the meshing for the Benchmark-I submarine model.

submarine at 215 Hz, with the direction of the incident wavefront parallel to the bow. **c** The corresponding results for the direction of the incident wavefront perpendicular to the bow.

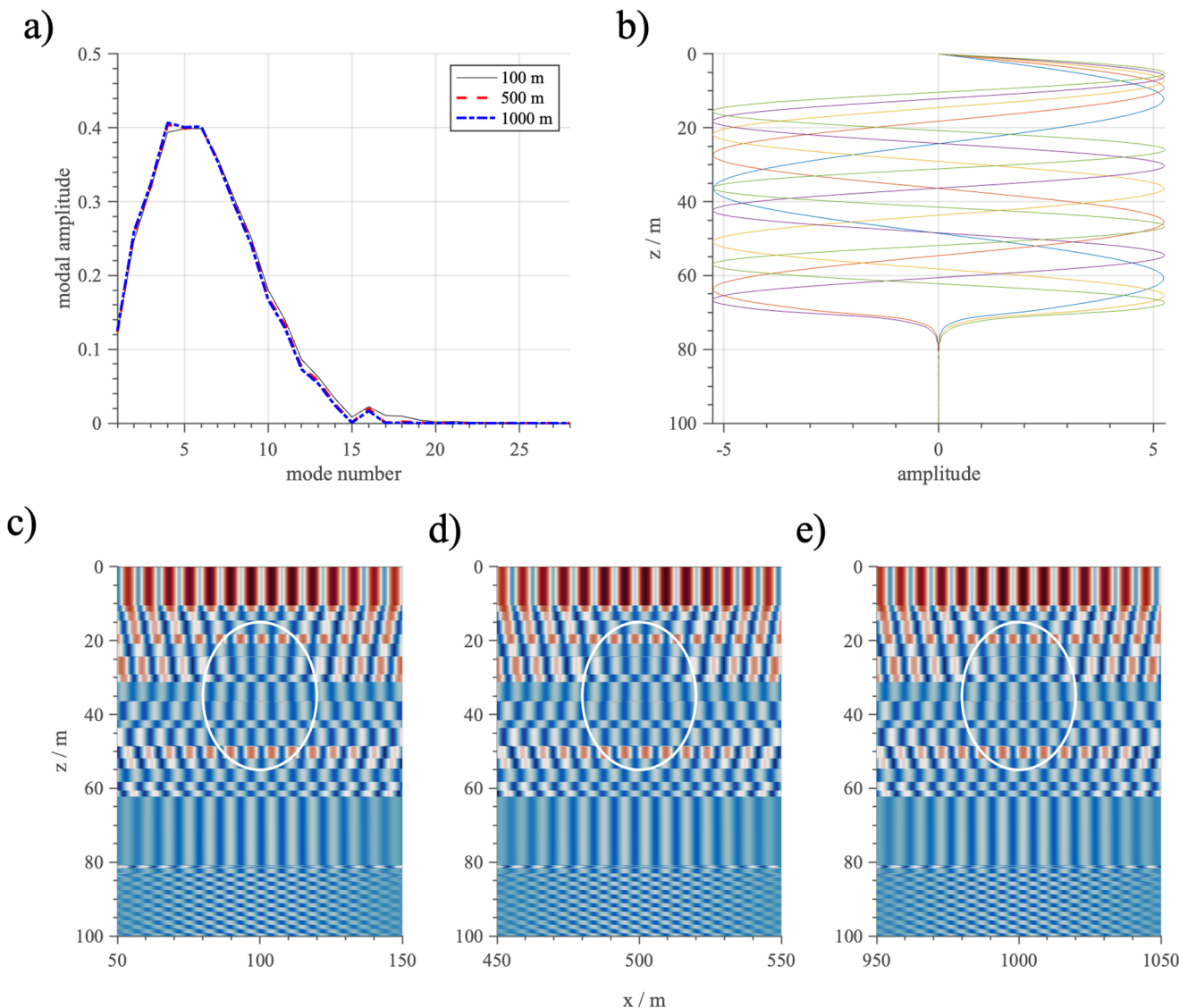


Fig. 7 | Modal amplitude and phase characteristics of the prescribed incident waves. **a** The modal amplitude distribution versus mode number at 215 Hz for different scatterer positions; **(b)** the modal shape functions of the dominant

mode group (modes 3–7); **(c–e)** the phase distribution of the dominant mode group for scatterer positions at 100 m, 500 m, and 1000 m.

Mechanism of incident field optimization

We now elucidate the mechanism underlying incident field optimization by analyzing backscattering suppression from the single steel spherical shell based on the result presented in Fig. 4a.

Typically, the prescribed incident wavefront depends on the scatterer position. Figure 4a reveals distinct prescribed incident wavefronts for different scatterer positions, despite similar beam patterns near the scatterer. A more direct illustration of the dependence of the prescribed incident wavefront on scatterer position is provided in Fig. 4b, which shows the incident wavefront profiles as a function of depth for three scatterer positions. Note that the incident wavefronts for 500 m and 1000 m share similarities in amplitude and phase. More interestingly, the modal amplitudes of these incident wavefronts are almost the same, as shown in Fig. 7a. The dominant mode group (modes 3–7) retains consistent amplitude weighting regardless of scatterer position. However, the modal phases vary spatially, enabling a Gaussian-like beam to bypass the scatterer. To illustrate this further, Fig. 7c–e shows the phase distribution obtained through coherent summation of the grouped modes for three different scatterer positions. Notably, the phases of the modes interfere constructively above the shell but destructively at depths below 50 m. This constructive

interference originates from the resonance of the first peaks in the mode shapes, as shown in Fig. 7b. The consistent interference pattern observed near the scatterer indicates that the system eigenfunctions remain unchanged under identical ocean environmental conditions. Translating the scattering region horizontally, while preserving its geometry and material composition, does not alter the dominant mode group responsible for reconstructing prescribed wavefronts and their corresponding modal amplitudes. However, the relative phases of these modes shift with the scattering region's horizontal position, resulting in a consistent wave pattern reconstruction deflecting around the scatterer.

Functioning as a modal filter, the scatterer serves as a secondary source that selectively excites specific propagating modes. This phenomenon elucidates the mechanism of mode coupling resulting from the non-uniform waveguide. Figure 8 presents a magnified view of the prescribed incident field (for scattering suppression) near the scatterer positioned at 500 m from the source, revealing a focused energy density profile that circumvents the spherical obstacle. This spatial alignment corresponds to the modal excitation characteristics of the incident field, determined by the grazing angles of modal plane waves. Prior research demonstrates that coupling of the source directivity with the waveguide field causes the former to function as a weighting

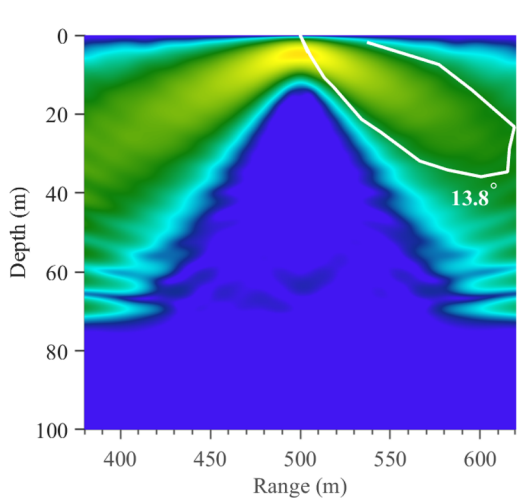


Fig. 8 | Wave pattern of the prescribed incident wavefronts near the scatterer. A magnified view of the optimal incident field bypassing the single spherical shell at 500 m, with modal excitation (source directionality) annotated as a function of modal plane-wave grazing angles.

Table 2 | Modal eigenvalues and grazing angles

Mode order	3	4	5	6	7
Eigenvalue	0.8913	0.8839	0.8743	0.8624	0.8481
Grazing angle (°)	8.25	11.04	13.87	16.73	19.65

factor for modal excitation⁸. Here, we quantify the modal excitation (i.e., the incident field's directionality) through its dependence on the grazing angles of modal plane waves, which is shown as a solid white line in Fig. 8.

Moreover, Table 2 summarizes the eigenvalues and grazing angles for modes 3–7, which correlate with the principal lobes in Fig. 8. The agreement between the incident-field patterns and modal excitation contours confirms that the prescribed incident wavefronts arise from the constructive modal interference localized at the scatterer's position.

Broadband backscattering manipulation

To demonstrate the broadband backscattering manipulation achieved via the proposed method, we simulate backscattering suppression and enhancement using a single steel spherical shell across a dimensionless frequency range ka (where a represents the scatterer's characteristic geometric dimension) from 4 to 25. Identical parameters to those in the single-sphere case are employed, including the scatterer and environmental configurations. The scatterer is positioned at coordinates (0 m, 500 m, 35 m).

We assess the broadband performance of the proposed method by computing G_r over a range of frequencies. Figure 9 illustrates G_r as a function of ka for suppression and enhancement scenarios. When the backscattering enhancement is implemented, G_r remains stable at approximately 50% across frequencies. In contrast, G_r generally increases under suppression conditions as the frequency decreases, marginally surpassing 1% at $ka = 4$. This may be caused by the beam broadening in the Gaussian-like path, which is intended to avoid the wave-scatterer interaction, becoming more pronounced with increasing wavelength. Conversely, the focusing for backscattering enhancement is less sensitive to wavelength variations within the dimensionless frequency range simulated. Despite this, Fig. 9 conclusively demonstrates that broadband backscattering manipulation can be achieved in ocean waveguides using the proposed methodology.

Influence of scatterer and environmental parameters

Finally, we examine the effects of parameters, including the scatterer's material and radius and seabed properties, on backscattering manipulation

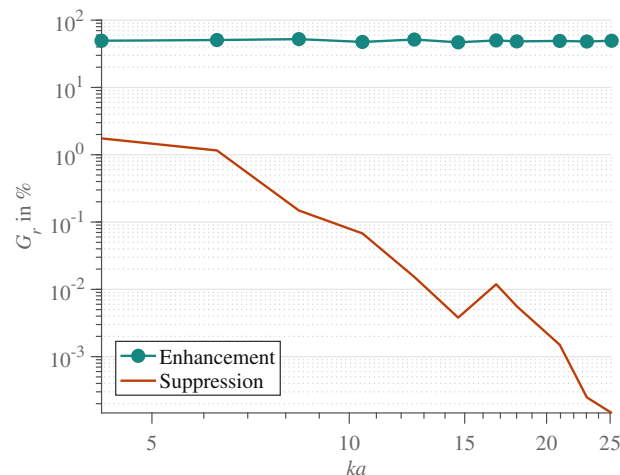


Fig. 9 | Broadband performance of the backscattering manipulation methodology. G_r as a function of the dimensionless frequency ka for backscattering enhancement (green dotted line) and suppression (red solid line) in the single-sphere case.

Table 3 | G_r for different scatter materials

Material	Enhancement	Suppression
Steel	48.2 %	0.0022%
Aluminum	47.9 %	0.0028%
Titanium	47.8 %	0.0026%

Table 4 | G_r for different scatterer radii

Radius	Enhancement	Suppression
15 m	33.1 %	2.78e-05%
10 m	20.9 %	6.29e-06%
5 m	4.3 %	2.15e-07%

for a spherical shell within the waveguide configuration detailed in Table 1. G_r quantifies the scattering enhancement or suppression across the FEM/NM coupling interface. Greater values of G_r are associated with stronger backscattering enhancement but weaker backscattering suppression, and vice versa. The scatterer is placed at (0 m, 500 m, 35 m). An incident frequency of 215 Hz is applied.

First, Table 3 compares G_r values for different scatterer materials under fixed geometric parameters (spherical shell with a radius of 20 m and a wall thickness of 0.1 m). The results indicate that backscattering enhancement yields a G_r at least four orders of magnitude greater than those for suppression, validating the method's effectiveness for controlling backscattering from objects in shallow water. Notably, G_r is insensitive to material properties, likely due to the source frequency operating below the shell's resonance frequency.

Next, Table 4 compares G_r values for different scatterer radii (ranging from 15 m to 5 m) under fixed material properties (steel spherical shell with a wall thickness of 0.1 m). The results indicate that larger geometric scales of scatterers are associated with significant backscattering enhancement but weak suppression. Notably, G_r plummets to only 4.34% when the radius decreases to 5 m, a scale comparable to the incident wavelength (approximately 7 m). At this threshold, diffraction effects dominate over scattering, overshadowing the backscattering and significantly reducing G_r , despite the implemented enhancement.

Finally, Table 5 compares G_r values for the same default scatterer (steel spherical shell with a radius of 20 m and a wall thickness of 0.1 m) located in

Table 5 | G_r for the same waveguide with different seabed types

Seabed	Enhancement	Suppression
Sand	48%	0.0025%
Basalt	48.1%	0.001%

waveguides with distinct seabed properties. Here, two additional seabeds are considered to evaluate how seabed hardness (linked to acoustic impedance) influences backscattering control: sand and basalt with sound speeds of 1700 m/s and 3500 m/s and densities of 1500 kg/m³ and 2700 kg/m³, respectively. Notably, stronger reflection is associated with a harder seafloor. The results demonstrate that seabed properties exert a negligible impact on G_r , with the values remaining consistent across configurations. This confirms the robustness of the proposed method in diverse ocean environments, supporting its applicability to practical underwater target detection scenarios.

Discussion

This study presents a theoretical analysis of backscattering manipulation for objects in shallow-water waveguides, potentially offering insights into a new paradigm for underwater acoustic detection and communication. The results indicate that broadband scattering manipulation in shallow-water waveguides can be achieved using the proposed method, with the reflection-to-incidence ratio increasing to nearly 50% under enhancement conditions or reducing to 2% when the suppression is implemented. The proposed mechanism hinges on reconstructing prescribed incident patterns near the scattering region through interference between specific modes. Under constant environmental conditions, the system's eigenfunctions remain the same; horizontal translation of the scatterer preserves the dominant mode group and modal amplitudes but induces phase shifts of these modes that reconfigure the same incident wave pattern near the scattering region. Parametric analyses reveal that the scatterer radius critically influences backscattering: larger radii amplify the backscattering strength, while smaller radii promote sound transmission through the waveguide. This work establishes a foundation for advanced active sonar strategies in shallow water, enabling the selective amplification of the backward or forward scattered field via prescribed wavefronts.

A critical question is how this approach can be applied in practice. To address this, more general underwater environments, featuring sound speed profiles (SSPs) and range-dependent topographies, must be considered. For water columns with depth-dependent SSPs, the proposed method can be extended directly, although a detailed analysis is beyond the scope of this study. The optimal incident wavefront remains valid for enhancing or suppressing the object's backscattering. However, when range-dependent SSPs are involved, the optimal incident wavefront derived from the SVD of \mathbf{R} may not maximize backscattering from the object, but rather from the environment, because the environment, being typically much larger in scale than the object, may dominate the backscattered signal. Similarly, in the presence of range-dependent topographies, the dominant right singular vector of \mathbf{R} may correspond to strong scattering from the seabed rather than the object. Nonetheless, an optimal incident wavefront for maximizing the object's backscattering still exists. It may be obtained by analyzing the first few largest singular values of \mathbf{R} . This remains an open problem and is the subject of our future research.

There are two potential ways of implementing the proposed method in practical applications. The first approach involves numerically evaluating all possible scenarios by varying the object's position within a fixed underwater environment (with known parameters). This requires substantial computational resources, as it necessitates repeated calculations of the matrices \mathbf{R} or \mathbf{T} for each possible scenario. After that, a set of candidate incident wavefronts can be tested to determine the one that yields the maximum backscattering or transmission. Another way involves blind estimation of \mathbf{R} or \mathbf{T} through in situ measurements. Although more challenging, the measurement approach

offers practical advantages. Obtaining \mathbf{R} or \mathbf{T} would require multiple measurements using blind estimation techniques²³ or inverse filtering²⁴, which remains an open research problem and will be a focus of our future work. In either way, acoustic emission relies on a phased array that spans the water column from the surface to the seabed. Such a requirement represents a major limitation of the proposed method. However, this limitation, the need for large apertures, may be mitigated in the future through array optimization or the use of state-of-the-art metamaterials exhibiting negative acoustic properties. For instance, underwater leaky wave antennas could serve as a promising alternative²⁵. These antennas are capable of producing acoustic radiation over a wide angular range (from -90° to 90°) and can be fabricated at significantly lower cost compared to conventional phased arrays by optimizing each individual element. Future efforts will focus on experimental reconstruction of modal-domain matrices using in situ measurements to detect scatterers at unknown locations.

Methods

Underwater sound propagation and the Sturm–Liouville eigenproblem

The wave propagation in the acoustic domain Ω_a is governed by the Helmholtz equation⁶

$$\nabla \left(\frac{1}{\rho} \nabla p \right) + \frac{\omega^2}{\rho c^2} p = 0, \quad (1)$$

where ρ is the density, and c is the sound speed. Consider a two-layer fluid waveguide. The boundary conditions for the waveguide system are defined as

$$\begin{cases} p(z)|_{z=0} = 0, \\ p(z)|_{z=h^-} = p(z)|_{z=h^+}, \\ \frac{1}{\rho(z)} \frac{\partial p(z)}{\partial z}|_{z=h^-} = \frac{1}{\rho(z)} \frac{\partial p(z)}{\partial z}|_{z=h^+}, \end{cases} \quad (2)$$

ensuring a pressure-release condition at the sea surface ($z = 0$) and continuity of the pressure and normal particle velocity across the water–seabed interface ($z = h$). To properly mimic a semi-infinite seabed, we introduce a PML extending from $z = D$ to H with a thickness of $d = H - D$. The pressure field is expressed via modal decomposition

$$p(r, z) = \sum_n a_n(r) \phi_n(z), \quad (3)$$

where ϕ represents the NM, the subscript n indicates the mode order, and a is the modal coefficient. The modes span the space onto which the pressure p is projected. Modal orthogonality is satisfied

$$\int_0^\infty \frac{1}{\rho(z)} \phi_n(z) \phi_m(z) dz = \delta_{nm}. \quad (4)$$

Theoretically, the integral in the above equation should be evaluated from $z = 0$ to $z = \infty$. However, the mode shape $\phi_n(z)$ decays with depth below the water–seabed interface; higher modes exhibit shallower depths at which the amplitude of $\phi_n(z)$ vanishes. Therefore, modal orthogonality remains valid for a finite depth D , defined as the depth where the lowest mode's amplitude approaches zero. In this study, we propose redefining modal orthogonality within a finite domain [0, D] by carefully choosing the maximal depth $z = D$ through a convergence test.

The $\phi_n(z)$ can be obtained by solving the Sturm–Liouville problem⁶

$$\frac{d^2 \phi}{dz^2} + \frac{\omega^2}{c^2} \phi = k_r^2 \phi, \quad (5)$$

subject to the boundary condition described by Eq. (2), but with $\phi_n(z)$ replacing $p(z)$. Here, k_r is the eigenvalue.

Such an eigen problem can be effectively solved using several established NM algorithms, including ORCA²⁶, rimLG²⁷, CAMBALA²⁸, Chebyshev spectral methods²⁹, and the widely used KRAKEN software³⁰. These approaches typically employ either finite-difference or spectral discretization techniques to solve the eigen equation described in Eq. (5), yielding both the eigenvalues and corresponding mode shape functions. A more detailed discussion of these models can be found in³¹.

In this study, the eigen problem is solved using a modal projection method^{18,32–34}, which is also known as the Fourier-Galerkin spectral method. A key advantage of this approach is its treatment of the continuous spectrum via high-order evanescent modes. Such a method with an appropriate treatment of the continuous spectrum is critical for near-field analyses to which such modes contribute significantly. This key aspect enables the incorporation of the NM with the FEM, the computational domain of the latter is typically of the scale of several acoustic wavelength. The method's implementation details are omitted here for brevity (see⁸ for further discussion).

Maximizing reflection and transmission in non-uniform waveguides

The governing equations above describe underwater sound propagation with range independency, indicating an absence of acoustic energy reflection within the system. Such waveguides are commonly referred to as uniform waveguides. Introducing a scatterer into this uniform environment induces backscattering phenomena. The region containing the scatterer then becomes non-uniform, leading to increased reflection and reduced transmission of sound waves.

In this study, the quantity used to characterize reflection and transmission in the waveguide is the squared pressure amplitude, $I = p^2$, which represents the *acoustic potential energy*⁵. Although this quantity is not the *acoustic intensity*, which represents the energy flux through a unit area per unit time, the subsequent derivation can be readily extended to *acoustic intensity* as well. We define the input I_{in} to a waveguide as

$$I_{\text{in}} = \int_0^D \frac{1}{\rho(z)} |p_{\text{in}}(z)|^2 dz = \mathbf{p}_{\text{in}}^H \boldsymbol{\Lambda} \mathbf{p}_{\text{in}}, \quad (6)$$

where p_{in} denotes the pressure distribution from $z = 0$ to $z = D$ at the waveguide entrance, and $\boldsymbol{\Lambda}$ represents the diagonal density matrix with elements $1/\rho(z)$. Note that although the integral in Eq. (6) theoretically requires sufficiently dense sampling of the water column to ensure modal orthogonality, it is not actually evaluated in practice when implementing reflection and transmission maximization. Instead, it is presented here to facilitate the subsequent derivation which further illustrates how reflection and transmission can be controlled through operations on \mathbf{R} and \mathbf{T} .

The corresponding output I_{out} is expressed as

$$I_{\text{out}} = \int_0^D \frac{1}{\rho(z)} |p_{\text{out}}(z)|^2 dz = \mathbf{p}_{\text{out}}^H \boldsymbol{\Lambda} \mathbf{p}_{\text{out}}, \quad (7)$$

where p_{out} represents the pressure distribution at the waveguide terminus.

Through the modal decomposition defined in Eq. (3), the input and output pressures become

$$\begin{aligned} \mathbf{p}_{\text{in}} &= \boldsymbol{\Phi} \mathbf{a}_{\text{in}}, \\ \mathbf{p}_{\text{out}} &= \boldsymbol{\Phi} \mathbf{T} \mathbf{a}_{\text{in}}, \end{aligned} \quad (8)$$

where \mathbf{T} is the transmission matrix mapping incident modal coefficients \mathbf{a}_{in} to output modal coefficients \mathbf{a}_{out} , and matrix $\boldsymbol{\Phi}$ contains the NMs.

The transmission-to-incidence ratio is given by:

$$G_t = \frac{I_{\text{out}}}{I_{\text{in}}} = \frac{\mathbf{p}_{\text{out}}^H \boldsymbol{\Lambda} \mathbf{p}_{\text{out}}}{\mathbf{p}_{\text{in}}^H \boldsymbol{\Lambda} \mathbf{p}_{\text{in}}}. \quad (9)$$

Substituting Eq. (8) into Eq. (9) yields

$$G_t = \frac{\mathbf{a}_{\text{in}}^H \mathbf{T}^H \boldsymbol{\Phi}^H \boldsymbol{\Lambda} \boldsymbol{\Phi} \mathbf{T} \mathbf{a}_{\text{in}}}{\mathbf{a}_{\text{in}}^H \boldsymbol{\Phi}^H \boldsymbol{\Lambda} \boldsymbol{\Phi} \mathbf{a}_{\text{in}}}. \quad (10)$$

Applying modal orthogonality (defined in a finite space from $z = 0$ to $z = D$ where the lowest mode's amplitude goes to zero) simplifies this to

$$G_t = \frac{\mathbf{a}_{\text{in}}^H \mathbf{T}^H \boldsymbol{\Lambda} \mathbf{T} \mathbf{a}_{\text{in}}}{\mathbf{a}_{\text{in}}^H \mathbf{a}_{\text{in}}}. \quad (11)$$

Maximizing acoustic transmission through the waveguide then corresponds to optimizing G_t , formulated as a Rayleigh quotient maximization

$$\arg \max_{\mathbf{a}_{\text{in}}} G_t = \arg \max_{\mathbf{a}_{\text{in}}} \sigma(\mathbf{T}^H \mathbf{T}) = \max(\sigma_t^2), \quad (12)$$

where σ_t are the singular values of \mathbf{T} from its singular value decomposition:

$$\mathbf{T} = \mathbf{U}_t \mathbf{S}_t \mathbf{V}_t^H, \quad (13)$$

with \mathbf{S}_t containing singular values σ_t in descending order, and \mathbf{U}_t , \mathbf{V}_t being unitary matrices of left and right singular vectors, respectively.

The optimal solution corresponds to the principal singular value $\sigma_{t,1}^2$, with its associated right singular vector $\mathbf{V}_{t,1}$ (first column of \mathbf{V}_t) providing the optimal modal coefficients for maximal sound transmission through the waveguide. This analysis demonstrates that strategic optimization of the incident wavefront prescription, guided by the principal singular vector of \mathbf{T} , suppresses backscattering in the waveguide.

To maximize acoustic reflection in waveguides, we define a reflection matrix \mathbf{R} that maps incident modal coefficients \mathbf{a}_{in} to backscattering modal coefficients \mathbf{a}_r . Following Eq. (12), the reflection optimization problem is formulated as

$$\arg \max_{\mathbf{a}_{\text{in}}} G_r = \arg \max_{\mathbf{a}_{\text{in}}} \sigma(\mathbf{R}^H \mathbf{R}) = \max(\sigma_r^2), \quad (14)$$

where G_r represents the reflection-to-incidence ratio, analogous to Eq. (11) with \mathbf{R} replacing \mathbf{T} . Here, σ_r denotes the singular values of \mathbf{R} , and the optimal solution corresponds to the principal right singular vector $\mathbf{V}_{r,1}$ associated with $\sigma_{r,1}$.

This formulation demonstrates backscattering control through incident wavefront prescription. We implement this theory by integrating the FEM with the NM method to compute \mathbf{R} and \mathbf{T} for shallow-sea waveguides containing arbitrary scatterers.

Two-step FEM scheme

When a scatterer is positioned in a shallow-water waveguide, the incident field inducing scattering typically exhibits non-planar wave characteristics, complicating scattered field modeling. To overcome this challenge, we propose a two-step FEM scheme whose computational results enable modal filtering for constructing \mathbf{R} and \mathbf{T} .

As shown in Fig. 1a, the acoustic scattering problem involves an elastic structure submerged in a waveguide, modeled using FEs. The structural domain Ω_s and the acoustic domain Ω_a are coupled at the interface Γ_{s-a} . The total scattered field \mathbf{p}_{tot} is decomposed into two components: geometric scattering \mathbf{p}_g , which is equivalent to the scattering from the same structure but with a rigid surface, and elastic scattering \mathbf{p}_e , which can be considered the radiation excited by the incident pressure \mathbf{p}_{inc} and the geometric scattered pressure \mathbf{p}_g . In this study, a two-step FEM scheme is proposed to solve \mathbf{p}_{tot} :

- Step 1: Solve \mathbf{p}_g using a pressure acoustics model (rigid boundary assumption).
- Step 2: Compute \mathbf{p}_e via a coupled acoustic-solid interaction model, where the elastic response is driven by \mathbf{p}_{inc} and \mathbf{p}_g .

This proposed two-step FEM scheme enables the calculation of scattered fields generated by non-plane wave excitations, which is critical for coupling FEM simulations with underwater acoustic propagation models. Figure 1b schematically illustrates the workflow of this two-step FEM framework.

First, an FE model for acoustic wave propagation is developed. The computational domain consists of a cylindrical region truncated by a PML, as illustrated in Fig. 1(a). The cylinder is partitioned at $z = h$, with the upper layer representing the water column and the lower layer corresponding to the seabed layer. The PML is applied to the outer cylindrical and bottom boundaries to mitigate spurious reflections. The wave propagation in the acoustic domain Ω_a is governed by the Helmholtz equation [Eq. (1)] subject to the boundary condition given by Eq. (2).

Applying FE discretization to the acoustic wave equation yields the linear system

$$[\mathbf{K}_a + j\omega \mathbf{D}_a - \omega^2 \mathbf{M}_a] \mathbf{p} = \mathbf{f}_a, \quad (15)$$

where \mathbf{p} denotes the nodal acoustic pressures, and \mathbf{K}_a , \mathbf{D}_a , and \mathbf{M}_a represent the stiffness, damping, and mass matrices for acoustics, respectively, as derived in⁶. The source term \mathbf{f}_a corresponds to external acoustic excitation.

The normal velocity boundary condition on the rigid surface satisfies

$$v_g = -v_{\text{inc}}, \quad (16)$$

where v_{inc} and v_g are the normal velocity components induced by the incident and geometry-scattered fields, respectively. In this work, v_{inc} is computed using a NM model⁸. By prescribing an inward normal velocity $-v_{\text{inc}}$ on the interface Γ_{s-a} , the FE solution provides the surface pressure load $\mathbf{p}_g + \mathbf{p}_{\text{inc}}$ on Γ_{s-a} .

Next, the pressure load $\mathbf{p}_g + \mathbf{p}_{\text{inc}}$ serves as input to the second FE model, which couples pressure acoustics with solid mechanics modules to compute the elastic scattering \mathbf{p}_e . In this coupled framework, the structural domain Ω_s and acoustic domain Ω_a are governed by the solid mechanics and pressure acoustics modules, respectively. The computational domain retains the geometry and boundary conditions (sea surface, water-seabed interface) defined in the initial acoustic FE model. The structural dynamics are described by⁶

$$(\lambda + \mu) \nabla (\nabla \cdot \hat{\mathbf{u}}) + \mu \hat{\mathbf{u}} + \rho \omega^2 \hat{\mathbf{u}} = 0, \quad (17)$$

where $\hat{\mathbf{u}}$ is the displacement vector, and λ , μ are Lam coefficients. Discretization yields the FE system

$$[\mathbf{K}_s + j\omega \mathbf{D}_s - \omega^2 \mathbf{M}_s] \mathbf{u} = \mathbf{f}_s, \quad (18)$$

where \mathbf{K}_s , \mathbf{D}_s , and \mathbf{M}_s are the stiffness, damping, and mass matrices for the solid mechanics, respectively, \mathbf{u} is the nodal displacement vector, and \mathbf{f}_s is the structural force.

Acoustic-structure coupling at Γ_{s-a} is enforced via³⁵

$$\begin{cases} \mathbf{f}_s = -\mathbf{F}\mathbf{p}, \\ \mathbf{v} = j\omega \mathbf{F}^T \mathbf{u}, \\ \mathbf{f}_a = \mathbf{p}_e + \mathbf{p}_g + \mathbf{p}_{\text{inc}}, \end{cases} \quad (19)$$

where \mathbf{F} is the coefficient matrix and \mathbf{v} is the normal velocity. The velocity-to-pressure transfer matrix is defined as

$$\mathbf{p}_e = j\rho\omega \mathbf{G}\mathbf{v}. \quad (20)$$

Substituting Eqs. (15) and (18) into Eq. (19) produces the coupled system

$$\begin{cases} [\mathbf{K}_s + j\omega \mathbf{D}_s - \omega^2 \mathbf{M}_s] \mathbf{u} + \mathbf{F}\mathbf{p} = 0, \\ \rho\omega^2 \mathbf{G}\mathbf{F}^T \mathbf{u} + [\mathbf{K}_a + j\omega \mathbf{D}_a - \omega^2 \mathbf{M}_a] \mathbf{p} = \mathbf{p}_g + \mathbf{p}_{\text{inc}}, \end{cases} \quad (21)$$

which in matrix form becomes

$$\left(\begin{bmatrix} \mathbf{K}_s & \mathbf{F} \\ 0 & \mathbf{K}_a \end{bmatrix} + j\omega \begin{bmatrix} \mathbf{D}_s & 0 \\ 0 & \mathbf{D}_a \end{bmatrix} - \omega^2 \begin{bmatrix} \mathbf{M}_s & 0 \\ \rho \mathbf{G} \mathbf{F}^T & \mathbf{M}_a \end{bmatrix} \right) \begin{bmatrix} \mathbf{u} \\ \mathbf{p} \end{bmatrix} = \begin{bmatrix} 0 \\ \mathbf{p}_g + \mathbf{p}_{\text{inc}} \end{bmatrix}. \quad (22)$$

Solving Eq. (22) with $\mathbf{p}_g + \mathbf{p}_{\text{inc}}$ applied as a pressure load on Γ_{s-a} yields \mathbf{p}_e . The total scattered field is the superposition of \mathbf{p}_e and \mathbf{p}_g .

Modal filter technique for the construction of R and T

After the two-step FEM scheme is established, the near-field scattered data $[\mathbf{p}_e$ and $\mathbf{p}_g]$ is extracted and used to construct \mathbf{R} and \mathbf{T} . We begin by first identifying the slice parallel to the incident wavefront, with its central axis identical to that of the FE model, as shown in Fig. 1a. Next, modal decomposition is applied to the near-field pressure distributed over a vertical line extending from $z = 0$ to $z = D$ in either the backscattered or forward-scattered directions

$$a_n = \int_0^D \frac{1}{\rho(z)} \phi_n(z) [p_e(z) + p_g(z)] / H_0^{(2)}(k_{r,n} r') dz, \quad (23)$$

where a_n are modal coefficients, with the subscript n indicating the coefficient of the n th normal mode. Here, r' indicates the horizontal range where the acoustic pressure is extracted for modal filtering. Each column of \mathbf{R} or \mathbf{T} requires sequential implementations of the two-step FEM with individual NMs as incident fields. The reflection matrix is defined as

$$\mathbf{R} = \begin{pmatrix} a_1^1 & a_1^2 & \dots & a_1^m & \dots & a_1^n \\ a_2^1 & a_2^2 & \dots & a_2^m & \dots & a_2^n \\ \vdots & \vdots & \ddots & \vdots & \ddots & \vdots \\ a_N^1 & a_N^2 & \dots & a_N^m & \dots & a_N^n \end{pmatrix}, \quad (24)$$

where the superscript m indicates excitation by the m th NM, and N is the total mode number. Reading column by column, this expression implies that the m th column of \mathbf{R} is computed by inputting the m th NM as the incident field $-v_{\text{inc},m}$ into the FE model to extract p_e^m and p_g^m in the backscattered direction. Then, the n th modal coefficient a_n^m excited by the m th mode can be calculated using Eq. (23). Full assembly of \mathbf{R} requires repetitive computation across all modes. The transmission matrix \mathbf{T} follows an analogous procedure but utilizes forward-scattered pressures.

The computation of the incident field $-v_{\text{inc},m}$ and the implementation of the modal filter technique for matrices \mathbf{R} and \mathbf{T} necessitate a NM model. We employ a modal projection method incorporated with PML to compute ϕ_n and $k_{r,np}$, which subsequently enable incident field derivation through the modal summation in Eq. (3).

A critical advantage of this approach lies in its accommodation of evanescent modes, which enables scattered field computation in the near-field region. This capability proves essential for integrating FEM and the NM algorithm, given the spatial constraints imposed by volumetric discretization of the computational domain. A more detailed discussion on determining mode number N for constructing \mathbf{R} and \mathbf{T} can be found in the Supplementary information.

The incident field $-v_{\text{inc},m}$ corresponding to the m th mode is expressed as

$$-v_{\text{inc},m} = -\left(n_x v_{\text{inc},x,m} + n_y v_{\text{inc},y,m} + n_z v_{\text{inc},z,m} \right) \quad (25)$$

where (n_x, n_y, n_z) denotes the surface normal vector, and the velocity components are defined by

$$\begin{cases} v_{\text{inc},x,m} = -\frac{x}{r} k_{r,m} \phi_m(z) H_1^{(2)}(k_{r,m} r) \\ v_{\text{inc},y,m} = -\frac{y}{r} k_{r,m} \phi_m(z) H_1^{(2)}(k_{r,m} r), \\ v_{\text{inc},z,m} = \frac{d\phi_m(z)}{dz} H_0^{(2)}(k_{r,m} r) \end{cases} \quad (26)$$

with $r = \sqrt{x^2 + y^2}$ representing the horizontal range coordinate. $-v_{\text{inc},m}$ is used as the input to the two-step FEM scheme, enabling the construction of the m th column of \mathbf{R} and \mathbf{T} .

Scattered field computation

After the construction of \mathbf{R} and \mathbf{T} , their SVD yields the incident fields maximizing and minimizing backscattering

$$p_{\text{inc}} = \Phi \mathbf{V}_{r/t,1} \mathcal{H}^{(2)}, \quad (27)$$

where the diagonal matrix $\mathcal{H}^{(1,2)}$ is defined as

$$\mathcal{H}^{(1,2)}(n, n) = H_0^{(1,2)}(k_{r,n} r). \quad (28)$$

The above incident field is then input into the two-step FEM scheme to compute the scattered field. The scattered fields outside the FE domain are computed by first performing the modal filtering [Eq. (23)] using the near-field data distributed over a vertical line extending from $z = 0$ to $z = D$ in either the backscattered or forward-scattered directions. The modal filtering gives the modal coefficient $a_{r/t}$ for backward or forward scattering, which can be used to calculate the far-field scattered fields based on the modal summation defined by Eq. (3)

$$p = \begin{cases} \Phi a_r \mathcal{H}^{(1)} & \text{(backward)} \\ \Phi a_t \mathcal{H}^{(2)} & \text{(forward)} \end{cases} \quad (29)$$

FEM implementation

The FE model is implemented using the commercial COMSOL Multiphysics software. A spherical scatterer with a radius of 20 m and a wall thickness of 0.1 m is considered initially. The shell is discretized using triangular meshes with a maximum element size of 1/60 the acoustic wavelength to resolve vibrational dynamics. Coarser meshes (1/6 the acoustic wavelength) are applied to the water and seabed domains. The computational domain is bounded by PMLs configured with a 10-layer mapping mesh. This meshing strategy ensures numerical convergence, as validated in prior studies³⁶. The shell material is modeled as structural steel (a Young's modulus of 2.09×10^{13} Pa, a Poisson's ratio of 0.269, and a density of 7890 kg/m³), enclosing a vacuum interior. The structural response and scattered pressure fields are solved using the solid mechanics and pressure acoustics physics interfaces, respectively, with acoustic-solid coupling implemented at the shell-water interface³⁷.

Data availability

All data and codes for reproducing the results presented in this paper are available upon reasonable request.

Received: 9 May 2025; Accepted: 22 September 2025;

Published online: 03 November 2025

References

1. Ainslie, M. A. *Principles of sonar performance modelling* Vol. 707 (Springer, 2010).
2. Hefner, B. T. & Marston, P. L. Backscattering enhancements associated with subsonic Rayleigh waves on polymer spheres in water: Observation and modeling for acrylic spheres. *J. Acoust. Soc. Am.* **107**, 1930–1936 (2000).
3. Blonigen, F. J. & Marston, P. L. Backscattering enhancements for tilted solid plastic cylinders in water due to the caustic merging transition: Observations and theory. *J. Acoust. Soc. Am.* **107**, 689–698 (2000).
4. Elliott, S., Orita, M., Quaranta, E. & Cheer, J. Acoustic scattering from spherical shells and its active control. *J. Sound Vib.* **568**, 118056 (2024).
5. Tan, L., Fan, J., Wang, B., Zhao, K. & Li, B. Backscattering enhancements by partially exposed spheres due to reflected subsonic Rayleigh waves at air–water interfaces. *J. Acoust. Soc. Am.* **153**, 1674–1681 (2023).
6. Jensen, F. B., Kuperman, W. A., Porter, M. B. & Schmidt, H. *Computational ocean acoustics*. Vol. 2011 (Springer, 2011).
7. Zhu, Y. et al. A nonlinear sound field control method for a multi-channel parametric array loudspeaker array. *J. Acoust. Soc. Am.* **157**, 962–975 (2025).
8. He, T. et al. Semi-analytical solution for sound propagation from a moving directional source in a shallow-water waveguide. *J. Sound Vib.* **576**, 118259 (2024).
9. Nie, R., He, T., Fan, J., Zhao, K. & Wang, B. Fast prediction of the long-range structural acoustic radiation in the stratified ocean. *Ocean Eng.* **314**, 119673 (2024).
10. Guo, W. & Yang, D.-S. Maximal transmission of acoustic energy flux in inhomogeneous waveguides and robustness analyses. *Acta Phys. Sin-Ch Ed.* **70**, 174302 (2021).
11. Zhang, H., Delaporte, T. & Ma, G. Scattering matrices of two-dimensional complex acoustic media. *npj Acoust.* **1**, 17 (2025).
12. Imry, Y. Active transmission channels and universal conductance fluctuations. *EPL-Europhys. Lett.* **1**, 249 (1986).
13. Pendry, J., MacKinnon, A. & Pretre, A. Maximal fluctuations—a new phenomenon in disordered systems. *Physica A* **168**, 400–407 (1990).
14. Dorokhov, O. Localization and transmission coefficient for two coupled metal chains with disorder. *Solid. State. Commun.* **44**, 915–919 (1982).
15. Popoff, S. M. et al. Measuring the transmission matrix in optics: An approach to the study and control of light propagation in disordered media. *Phys. Rev. Lett.* **104**, 100601 (2010).
16. Kim, M. et al. Maximal energy transport through disordered media with the implementation of transmission eigenchannels. *Nat. Photonics.* **6**, 581–585 (2012).
17. Popoff, S. M., Goetschy, A., Liew, S., Stone, A. D. & Cao, H. Coherent control of total transmission of light through disordered media. *Phys. Rev. Lett.* **112**, 133903 (2014).
18. Nazarov, Y. V. Limits of universality in disordered conductors. *Phys. Rev. Lett.* **73**, 134 (1994).
19. Hein, S., Koch, W. & Nannen, L. Fano resonances in acoustics. *J. Fluid. Mech.* **664**, 238–264 (2010).
20. Hein, S., Koch, W. & Nannen, L. Trapped modes and fano resonances in two-dimensional acoustical duct–cavity systems. *J. Fluid. Mech.* **692**, 257–287 (2012).
21. Xiong, L., Bi, W. & Aurégan, Y. Fano resonance scatterings in waveguides with impedance boundary conditions. *J. Acoust. Soc. Am.* **139**, 764–772 (2016).
22. Bonnet-Ben Dhia, A.-S. & Nazarov, S. Obstacles in acoustic waveguides becoming “invisible” at given frequencies. *Acoust. Phys. +* **59**, 633–639 (2013).
23. Cang, S., Swärd, J., Sheng, X. & Jakobsson, A. Toeplitz-based blind deconvolution of underwater acoustic channels using wideband integrated dictionaries. *Signal. Process.* **179**, 107812 (2021).
24. Fink, M. Time reversal of ultrasonic fields. I. Basic Principles. *IEEE T. Ultrason Ferr.* **39**, 555–566 (2002).
25. Broadman, C. W., Naify, C. J., Lee, M. J. & Haberman, M. R. Design of a one-dimensional underwater acoustic leaky wave antenna using an elastic metamaterial waveguide. *J. Appl. Phys.* **129**, 194902 (2021).
26. Westwood, E. K., Tindle, C. T. & Chapman, N. R. A normal mode model for acousto-elastic ocean environments. *J. Acoust. Soc. Am.* **100**, 3631–3645 (1996).
27. Evans, R. rimlg: A Legendre–Galerkin technique for differential eigenvalue problems with complex and discontinuous coefficients, arising in underwater acoustics. *Ocean Acoustics Library* <https://oalib-acoustics.org/models-and-software/normal-modes/> (2020).

28. Tyshchenko, A., Zaikin, O., Sorokin, M. & Petrov, P. A program based on the wide-angle mode parabolic equations method for computing acoustic fields in shallow water. *Acoust. Phys.* **67**, 512–519 (2021).
29. Tu, H. et al. A Chebyshev-Tau spectral method for normal modes of underwater sound propagation with a layered marine environment. *J. Sound Vib.* **492**, 115784 (2021).
30. Porter, M. The KRAKEN normal mode program. Saclant Undersea Research Centre <https://oalib-acoustics.org/models-and-software/normal-modes> (2001).
31. Wang, Y., Tu, H., Xu, G. & Gao, D. A review of the application of spectral methods in computational ocean acoustics. *Phys. Fluids* **35**, 121301 (2023).
32. He, T., Mo, S., Guo, W. & Fang, E. Modeling propagation in shallow water with the range-dependent sea surfaces and fluid seabeds using the equivalent source method. *J. Acoust. Soc. Am.* **149**, 997–1011 (2021).
33. He, T., Liu, J., Ye, S., Qing, X. & Mo, S. A novel model order reduction technique for solving horizontal refraction equations in the modeling of three-dimensional underwater acoustic propagation. *J. Sound Vib.* **591**, 118617 (2024).
34. He, T., Mo, S. & Qing, X. Semi-analytical solution for three-dimensional underwater acoustic propagation from a directional source. *J. Sound Vib.* **618**, 119253 (2025).
35. Xie, X. & Liu, Y. Efficient multi-frequency solutions of FE–BE coupled structural–acoustic problems using Arnoldi-based dimension reduction approach. *Comput. Methods Appl. Mech. Engrg.* **386**, 114126 (2021).
36. Isakson, M. J. & Chotiros, N. P. Finite element modeling of reverberation and transmission loss in shallow water waveguides with rough boundaries. *J. Acoust. Soc. Am.* **129**, 1273–1279 (2011).
37. An, B., Zhang, C., Shang, D., Xiao, Y. & Khan, I. U. A combined finite element method with normal mode for the elastic structural acoustic radiation in shallow water. *J. Theor. Comput. Acous.* **28**, 2050004 (2020).

Acknowledgements

This work was supported by the National Natural Science Foundation of China (Grant No. 12304499).

Author contributions

T.H. led the conceptualization and formulation of the method, served as a primary author, and supervised code implementation, results visualization,

and manuscript writing. W.G. contributed substantially to method development and to the review and revision of the manuscript.

Competing interests

The authors declare no competing interests.

Additional information

Supplementary information The online version contains supplementary material available at <https://doi.org/10.1038/s44384-025-00033-6>.

Correspondence and requests for materials should be addressed to Tengjiao He or Wei Guo.

Reprints and permissions information is available at <http://www.nature.com/reprints>

Publisher's note Springer Nature remains neutral with regard to jurisdictional claims in published maps and institutional affiliations.

Open Access This article is licensed under a Creative Commons Attribution-NonCommercial-NoDerivatives 4.0 International License, which permits any non-commercial use, sharing, distribution and reproduction in any medium or format, as long as you give appropriate credit to the original author(s) and the source, provide a link to the Creative Commons licence, and indicate if you modified the licensed material. You do not have permission under this licence to share adapted material derived from this article or parts of it. The images or other third party material in this article are included in the article's Creative Commons licence, unless indicated otherwise in a credit line to the material. If material is not included in the article's Creative Commons licence and your intended use is not permitted by statutory regulation or exceeds the permitted use, you will need to obtain permission directly from the copyright holder. To view a copy of this licence, visit <http://creativecommons.org/licenses/by-nc-nd/4.0/>.

© The Author(s) 2025